Defect-induced Burstein-Moss shift in reduced V_2O_5 nanostructures

Qi Wang,[1] Mathew Brier,[1] Siddharth Joshi,[1] Ajinkya Puntambekar,[1] and Vidhya Chakrapani[1,2,*]

[1]*Howard P. Isermann Department of Chemical and Biological Engineering, Rensselaer Polytechnic Institute, Troy, New York 12180, USA*

[2]*Department of Physics, Applied Physics, and Astronomy, Rensselaer Polytechnic Institute, Troy, New York 12180, USA*

(Received 28 June 2016; revised manuscript received 25 September 2016; published 13 December 2016)

The main effects of oxygen vacancy defects on the electronic and optical properties of V_2O_5 nanowires were studied through *in situ* Raman, photoluminescence, absorption, and photoemission spectroscopy. Both thermal reduction and electrochemical reduction via lithium insertion leads to the creation of oxygen vacancy defects in the crystal that gives rise to new electronic midgap defect states at energy 0.75 eV below the conduction band edge. The defect formation results in delocalization and injection of excess electrons into the conduction band, as opposed to localized electron injection as previously suggested. Contrary to what is seen in most oxides, the presence of vacancy defects leads to band filling and an increase in the optical band gap of V_2O_5 from 1.95 to 2.45 eV, which is attributed to the Burstein-Moss effect. Other observed changes in the optical properties are correlated to the changes in the electronic structure of the oxide as a result of defect formation. Further, *in situ* Raman measurements during the electrochemical reduction at room temperature show that the oxygen atom that is most readily reduced is the threefold coordinated oxygen (O3).

DOI: 10.1103/PhysRevB.94.245305

Among the various transition metal oxides (TMOs), oxides of vanadium, especially vanadium pentoxide (V_2O_5), are unique for several reasons: (i) V_2O_5 is one of the most easily reduced TMOs with vanadium existing in a variety of oxidation states in its various reduced phases, such as V^{+2} as in VO, V^{+3} in V_2O_3, or V^{+4} in VO_2. Hence, they are widely used as amphoteric catalysts [1,2] for many industrial reactions, such as selective oxidation and reduction of hydrocarbons, oxidation of SO_2 to SO_3, selective reduction of nitric oxide, and many others, in addition to being effective photocatalysts [3]. (ii) The highly layered orthorhombic structure of V_2O_5 with a weak van der Waals interaction between layers makes it valuable for monolayer devices [4] and host electrodes for ion intercalation in batteries [5], sensors [6], and smart materials [7]. In most of these applications, V_2O_5 undergoes reduction as a result of formation of oxygen vacancy V_O defects. It is these defects which impact many of the functional properties characteristic of the oxide, such as enhancement of catalytic activity by acting as hotspots for adsorptive binding of chemical species [8] or by impacting electronic properties that result in metal-to-insulator transitions [9]. Thus, understanding the effects of V_O on the electronic properties is important for elucidating the structure-property-function of metal oxides.

Reduction of V_2O_5 through the formation of oxygen vacancy V_O defects have been studied both by theoretical and experimental studies [10–15]. It is generally known that the presence of V_O defects causes a change in the oxidation state of neighboring vanadium atoms from V^{+5} to V^{+4} or lower states [16]. In addition, ultraviolet photoemission spectroscopy (UPS) studies show the formation of new midgap states as a result of reduction based on the appearance of a board peak centered at 1.3 eV above the valence band (VB) edge [17,15]. Some disparity exists in the results of theoretical calculations of reduced oxide. Density functional theory (DFT) cluster work of Hermann *et al.* [18] reported the reduction of neighboring vanadium atoms that led to increased V 3*d* orbital occupation. No distinct peaks related to V_O defects in the band gap were reported. Gradient-corrected DFT + *U* calculations of Scanlon *et al.* [11] showed the creation of new gap states 0.7–1.0 eV above the VB edge for various oxygen vacancy defects. These reports do not indicate any shift in the band gap of reduced V_2O_5 or band filling. It was suggested that V_O defects result in increase in electron concentration that is localized on vanadium atoms in the vicinity of the vacancy. Separately, the nature of oxygen vacancy, *i.e.* the oxygen that is most readily lost during catalytic reduction, has been well studied and debated [8,11,18,19]. The primitive cell of orthorhombic V_2O_5 consists of three crystallographically distinct oxygen atoms: the singly coordinated oxygen (O1) atom which forms vanadyl group V = O, and double- or triple-coordinated bridging oxygen atoms (O2 and O3, respectively). Though there is no clear consensus, it has been generally believed that it is the O1 oxygen atom that is most readily lost and thus most important for the catalytic reactions [11,14].

On the other hand, the effects of electrochemical reduction of V_2O_5 by Li^+ intercalation have been well studied from the perspective of electrochromic devices [20,21]. Here, V_2O_5 is known to exhibit double electrochromic effect, wherein intercalation of Li^+ ions is known to cause a decrease in the absorbance in the ultraviolet (UV) spectral region with a shift in the optical absorbance edge and an increase in absorbance in the near-infrared (NIR) region [20,21]. The blueshift of the absorption edge was attributed to the Burstein-Moss effect occurring as a result of band filling. It has been generally accepted that rise in the NIR absorbance in lithiated oxide is due to the absorption by polarons [20], though photoelectron spectroscopy studies show that appearance of a peak in the UPS spectrum [22] at ∼1.1 eV above the VB maximum and electron paramagnetic resonance studies [12] suggest the vacancy defects may be responsible for NIR absorption. Electron nuclear double resonance by Pecquenard *et al.* [23] suggests that polarons, including bound ones trapped on four vanadium sites around the Li^+ ions and free polarons around a single vanadium site, give rise to NIR absorption. Theoretical work of Jiang *et al.* [24], on the other hand, have predicted

*chakrv@rpi.edu

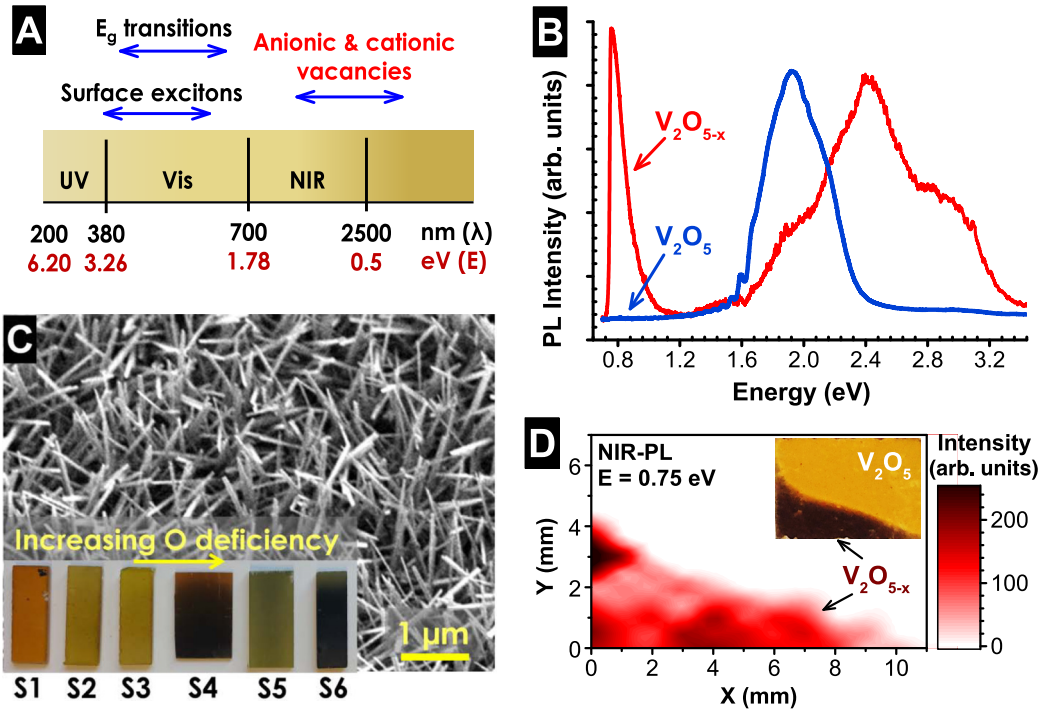

FIG. 1. (A) Energy range of the various radiative transitions in vanadium oxide spanning from UV to NIR spectral region. (B) Representative emission spectra of nonstoichiometric vanadium oxide (V_2O_{5-x}) and stoichiometric (V_2O_5) upon excitations with 633 and 325 nm lasers in the energy range of 0.7–1.3 eV and 1.3–3.3 eV, respectively. (C) SEM image of single crystal V_2O_5 nanowires grown on FTO substrates. Inset: Optical images of vanadium oxide samples with increasing oxygen deficiency. (D) Optical micrograph and the corresponding NIR-PL map taken at emission energy of 0.75 eV of an oxide surface consisting of oxidized (V_2O_5) and reduced (V_2O_{5-x}) oxide. The region of V_2O_{5-x} containing V_O defects shows a strong NIR emission, while the V_2O_5 region shows no detectable NIR emission.

metallic conductivity for $Li_xV_2O_5$ even for small values of x and attribute the absorbance to free carrier absorption.

In this paper, we address some of the key unanswered questions regarding the correlation between optical properties and electronic structure of V_2O_5 reduced by two methods: thermal reduction and electrochemical reduction with Li^+. We show that both processes result in the generation of a high density of V_O defect-related electronic states ~0.75 eV below the conduction band (CB) edge and with a corresponding increase in the optical band gap as a result of the defect-induced Burstein-Moss shift, which is in contrast to what is seen in most oxides of transition metal, including vanadium. As a general trend, the band gap of oxide decreases with increasing oxygen vacancy or reduction, which is evident in the various reduced phases of vanadium oxide whose band gap narrows from 2.0 eV seen in V_2O_5 to 0.7 eV in VO_2 to 0.4 eV in V_2O_3 and no gap in VO [13,25]. The rise of absorbance in the NIR spectral range in reduced oxide is a result of optical excitation of V_O defect-related midgap states. In addition, using *in situ* Raman measurements during the reduction process, we show that the oxygen atom that most readily participates during electrochemical reduction at room temperature and gets reduced is the threefold coordinated oxygen (O3).

Vacancies in vanadium oxide have been probed using a variety of spectroscopic techniques, such as scanning tunneling microscopy [9,26,27], electron energy loss spectroscopy [28,29], electron paramagnetic resonance studies [16,12,23], x-ray absorption measurements [30], and x-ray photoemission spectroscopy (XPS) [15,17]. However, most of these techniques either require ultrahigh vacuum (UHV) or a controlled environment for operation that makes it difficult to adapt it to *in situ* catalytic studies. Here, we use NIR photoluminescence (NIR-PL) and Raman spectroscopy that allows for study of vacancy defects and their interaction with redox species under *in operando* electrochemical conditions at room temperature, as shown in our recent paper [31]. The spectral range of various types of electronic transitions in V_2O_5 is shown in Fig. 1(A). Representative PL spectra of stoichiometric and nonstoichiometric V_2O_5 are shown in Fig. 1(B). The optical gap of nominally undoped V_2O_5 is in the range of 1.9–2.5 eV, and hence, emission spectrum lies in the UV-to-visible part of the spectral range. In most TMOs, deviation from stoichiometry is a result of the presence of a high density of either cationic or anionic vacancies in the lattice. The presence of vacancy defects gives rise to additional electronic states within the band gap. In general, both types of vacancies upon optical excitation give rise to radiative emissions that lie in the NIR region of the spectrum. This NIR emission provides a direct tool for probing vacancy formation or passivation by adsorbates or redox species. Here, V_2O_5, being one of the most easily reducible oxides, has the propensity to form oxygen vacancy V_O defects, which can render the crystal nonstoichiometric. From the PL spectra in the NIR spectral region shown in Fig. 1(B), the presence of V_O defects causes a NIR emission whose peak intensity is centered at 0.75 eV, while fully oxidized V_2O_5 shows no NIR radiative emission. In this paper, we show with the combination of both UV-to-NIR-PL and absorption spectroscopy that the formation

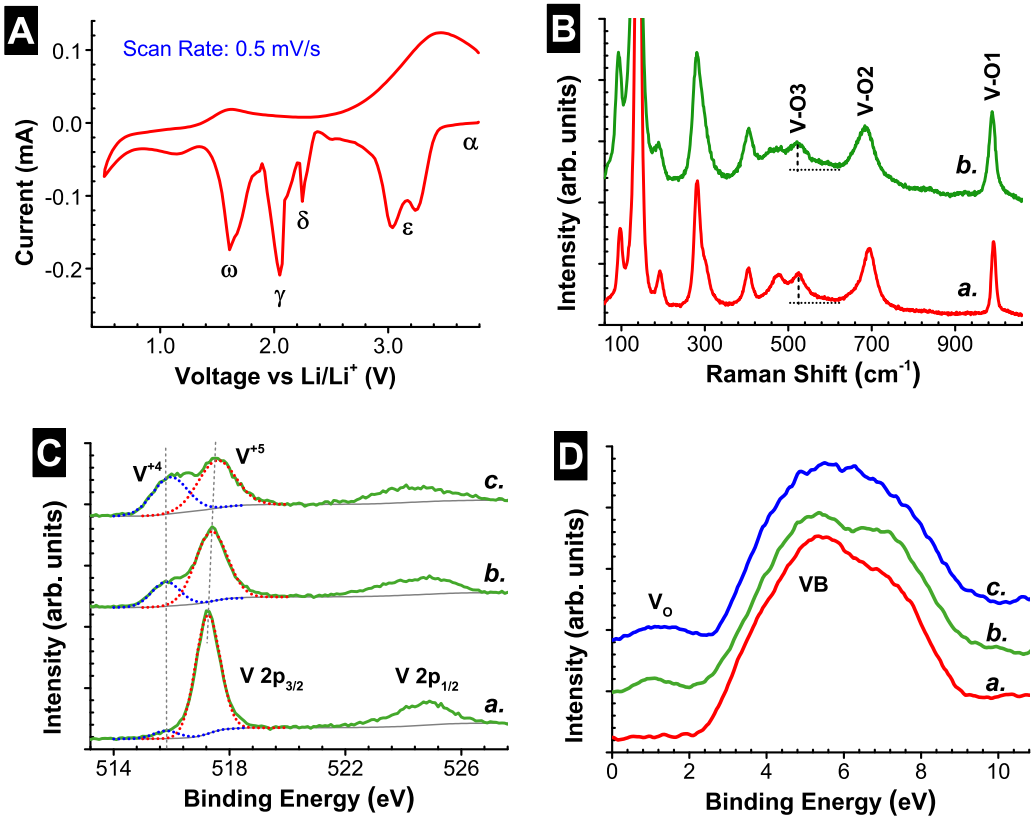

FIG. 2. (A) Cyclic voltammogram of α-V_2O_5 during electrochemical cycling in 0.1 M $LiClO_4$ in propylene carbonate taken at a scan rate of 0.5 mV/s. The peaks in the voltammogram correspond to the phase transformation of V_2O_5 to various lithiated phases due to Li^+ intercalation. (B) *in situ* Raman spectra of V_2O_5 at open circuit potential (OCP, curve *a*) and at potential of 3.2 V vs Li/Li^+ (curve *b*). Raman peak at 528 cm^{-1} corresponding to the vanadium bonded to bridging oxygen (O3) shows the largest decrease in the intensity, which suggests that O3 oxygen is the most easily reduced. (C) XPS spectra of V 2*p* core level before (curve *a*) and after Li^+ insertion (curves *b* and *c*) at potentials 3.2 and 2.5 V, respectively. The increase in the intensity peak corresponding to V^{+4} is evident in the lithiated samples. (D) Low-binding energy valence spectra showing the development of a new peak at ~1 eV as a result of Li^+ insertion.

of anionic defects by both thermal and electrochemical reduction leads to a Burstein-Moss shift in the optical band gap of V_2O_5.

Vanadium oxide nanowires of varying stoichiometry were prepared by the hot filament chemical vapor deposition (HFCVD) technique, which is described in detail in the Appendix. Nanowires with a range of vanadium-to-oxygen ratios were prepared with high purity without the introduction of extraneous reducing agents by simply tuning the filament power and partial pressure of oxygen and water vapor in the chamber, as was shown in our recent paper for other oxides [32,33]. Figure 1(C) shows the scanning electron micrograph (SEM) of as-synthesized oxide grown on fluorinated tin oxide (FTO) substrates. From the image, the as-synthesized deposits are seen to be vertically aligned, single crystalline nanowires with diameters in the range of 60–80 nm and length extending to 1–2 μm. As is common in most TMOs, the color of the sample provides a visual measure of the extent of deviation from stoichiometry [32]. In vanadium oxide, the fully stoichiometric phase (V_2O_5) is orange in optical coloration, while increasing oxygen deficiency shifts the sample color sequentially from orange to yellow-brown to dark green to the grayish-black seen in the highly reduced V_2O_{5-x} phase. Six samples, referred to here as S1 to S6, were prepared with increasing oxygen deficiency, consisting of stoichiometric V_2O_5 (orange, S1) to highly reduced V_2O_{5-x} phase (yellow to black, S2 to S6). Optical images of these six samples are shown in the inset of Fig. 1(C). Figure 1(D) shows an optical image and the corresponding NIR-PL map taken at emission energy of 0.75 eV of an oxide surface consisting of the V_2O_5 and V_2O_{5-x} phases excited using a subband gap light of 633 nm wavelength. The stoichiometric phase is orange in optical coloration with no detectable NIR emission, while increasing nonstoichiometric phases shows dark brown coloration and a strong NIR emission due to the presence of V_O defects.

Electrochemical reduction of stoichiometric V_2O_5 was performed in a three-electrode cell with application of a negative bias with respect to (w.r.t.) a Li/Li^+ reference and counter electrode in an electrolyte containing 0.1 M $LiClO_4$ in propylene carbonate. The Li^+ intercalation into V_2O_5 results in a multistep reduction and phase transformation, which has been studied in detail before [20]. Figure 2(A) shows the cyclic voltammograms taken at a slow scan rate of 0.5 mV/s of stoichiometric V_2O_5 during the first electrochemical reduction-oxidation cycle with a sequential formation of various V_2O_5 phases (also known as bronzes) due to Li^+ intercalation. Sharp peaks in the voltammogram seen at various potentials are indicative of phase transformation to various phases and are

similar to the ones reported in the literature [20]. For example, the peak in the current density seen at 3.1 V vs Li/Li^+ is a result of phase transformation from α-V_2O_5 to ε-$Li_{0.5}V_2O_5$. Progressive insertion of Li^+ leads to the formation of δ-LiV_2O_5 and γ-$Li_2V_2O_5$ phases, which occurs at a potential of around 2.3 and 2.0 V vs Li/Li^+, respectively. Further intercalation results in the formation of ω-$Li_3V_2O_5$ at 1.6 V vs Li/Li^+. The formation of γ-LiV_2O_5 and lower phases at potentials below 2 V are irreversible due to the structural changes that the lattice has to undergo in order to accommodate more than two lithium atoms per unit cell. Structural and electronic shifts caused by Li^+ insertion at various electrochemical potential were probed by *in situ* Raman PL, *ex situ* XPS, and absorption measurements in the UV-to-NIR spectral range. All electrochemical potential mentioned here are with respect to the reference potential of Li/Li^+ that has a standard electrode potential of -3.05 V versus a standard hydrogen electrode [34]. In addition to nanowire samples, experiments were also repeated with commercially available micron-sized powders of V_2O_5. No major differences in the results were seen between nanowires and microparticles.

Crystalline V_2O_5 forms an orthorhombic layered structure along the c axis of the unit cell and belongs to the space group of $Pmmn$ ($a = 11.510$ Å, $b = 4.369$ Å, $c = 3.563$ Å). The primitive cell contains four V atoms and 10 O atoms that correspond to two stoichiometric V_2O_5 units. Each layer consists of a periodic arrangement of edge-sharing and corner-sharing distorted trigonal VO_5 pyramids, and the layers are held together by weak vanadium-oxygen van der Waals interactions. Three different types of oxygen bonding exist within the V_2O_5 structure: terminal vanadyl oxygen (V = O1), double bridging oxygen to two vanadium sites, and triple bridging oxygen [11]. The nearest neighbors of each vanadium atom form a distorted octahedron in which one vanadyl-oxygen bond (V = O1) oriented perpendicular to the (001) plane is unusually short (1.58 Å), and another that consists of vanadium bonded to an oxygen atom in an adjacent layer is unusually long (2.79 Å). The bridging oxygen (denoted as O2) connects two adjacent vanadium atoms with two V-O bond lengths of 1.77 Å, and threefold coordinated oxygen (denoted as O3) with three V-O bond lengths of 1.88, 1.88, and 2.02 Å [35]. Figure S1 in the Supplemental Material [36] shows the schematic of coordination of vanadium ion in V_2O_5.

Here, V_2O_5 is a very effective catalyst for many important reactions because of the ease with which it loses the lattice oxygen in many oxidative reactions. The resulting oxygen vacancies, associated with the three distinct lattice oxygen atoms, play a crucial role in catalytic reaction by acting as hotspots for adsorptive binding of reacting species. Several detailed studies have been undertaken using various theoretical and spectroscopic tools to elucidate the nature of oxygen that most readily participates in catalytic reactions [11,16,19,37,38]. However, there is no clear consensus yet on the results of these studies. The computed theoretical density of states (DOS) by DFT calculations, which are in agreement with the results from angle-resolved UPS (ARUPS), show that the three differently coordinated oxygen atoms contribute to different regions of the VB states [39]. Density of states contributed by terminal vanadyl oxygen (O1) are localized near the center of the VB, whereas those of two- and threefold bridging oxygen (O2 and O3) yield a broad distribution spanning the full width of the VB and peaking near the periphery. Angle-resolved UPS results of Hermann *et al.* [18] on the reaction of V_2O_5 (010) with hydrogen showed that hydrogen affected peripheral VB DOS more than the states from the central region. Hence, they concluded that bridging oxygen atoms (O2 and O3) most readily react with adsorbed H_2 to create oxygen vacancies, as these oxygen atoms are more weakly bound to the surface than terminal oxygen (O1). A similar conclusion was drawn from the IR spectroscopic results of Ramirez *et al.* [19] that relative changes in the intensity of vibration stretches corresponding to O3 and O2 compared to the O1 stretch of V_2O_5 during reaction with dimethyl sulfoxide at 123 °C. In both these studies, distinction could not be made between the reactivity of O2 and O3 bridging oxygen atoms. Similarly, Tepper *et al.* [40] studied the reactivity of the unsupported V_2O_5 surface towards atomic hydrogen through high-resolution electron energy loss spectroscopy (HREELS) and ARUPS techniques and concluded that the most reactive oxygen atom is the bridging oxygen, while terminal and threefold coordinated sites are stable with respect to the interaction of atomic hydrogen. In contradiction to these results, both prior [14,41,42] and recent [11] theoretical calculations by several researchers noted that the formation energy of O1 vacancy is the lowest compared to O2 and O3 vacancies based on gradient-corrected DFT + U results and concluded that the O1 vacancy is the most stable defect and thus the most likely to be active during a reduction reaction. Further UPS results of Wu *et al.* [17] during thermal reduction of V_2O_5 showed a decrease in the intensity of both the central and top regions of the VB during reduction in contradiction to the results of Hermann *et al.* Studies by Ozkan *et al.* [42] on the reducibility of V_2O_5 with H_2 and NH_3 by temperature programmed desorption also showed that the interaction of reducing agents occurs primarily with the terminal vanadyl (O1) oxygen atom. In all, significant disparity exists in the results reported in the literature to conclusively assign the nature of O vacancy. In addition to the above reports, a significant number of in-depth catalytic studies has been performed on supported V_2O_5. The effect of support is also of great importance because of the presence of reactive sites at the interface of oxide and support [43–47]; hence, the results from supported catalysts cannot be extended to unsupported V_2O_5 catalysts.

In this paper, we use Raman spectroscopy to study the relative reactivity of the three different lattice oxygen atoms towards Li^+ ions to identify the one that is most readily reduced electrochemically at room temperature. Reaction of Li^+ with various lattice oxygen atoms results in the formation of Li-O [48] or Li_2O and a V_O defect. Raman spectroscopy is a powerful and sensitive tool for studying structural and bonding changes occurring in oxide and has been widely used for *in situ* gas-phase catalytic studies [45–47,49]. The technique can show distinct peaks for the Raman-active bending and stretching modes of the three different V-O bonds and thus can distinguish between reactivity of various oxygen atoms. Curve *a* in Fig. 2(B) shows typical Raman spectra of stoichiometric V_2O_5. Raman peaks at ν-996 cm^{-1}, δ-407 cm^{-1}, and δ-285 cm^{-1} correspond to the terminal vanadyl oxygen (V = O1), where ν denotes stretching and δ represents the bending modes of vibration, respectively. Peaks at ν-702 cm^{-1}

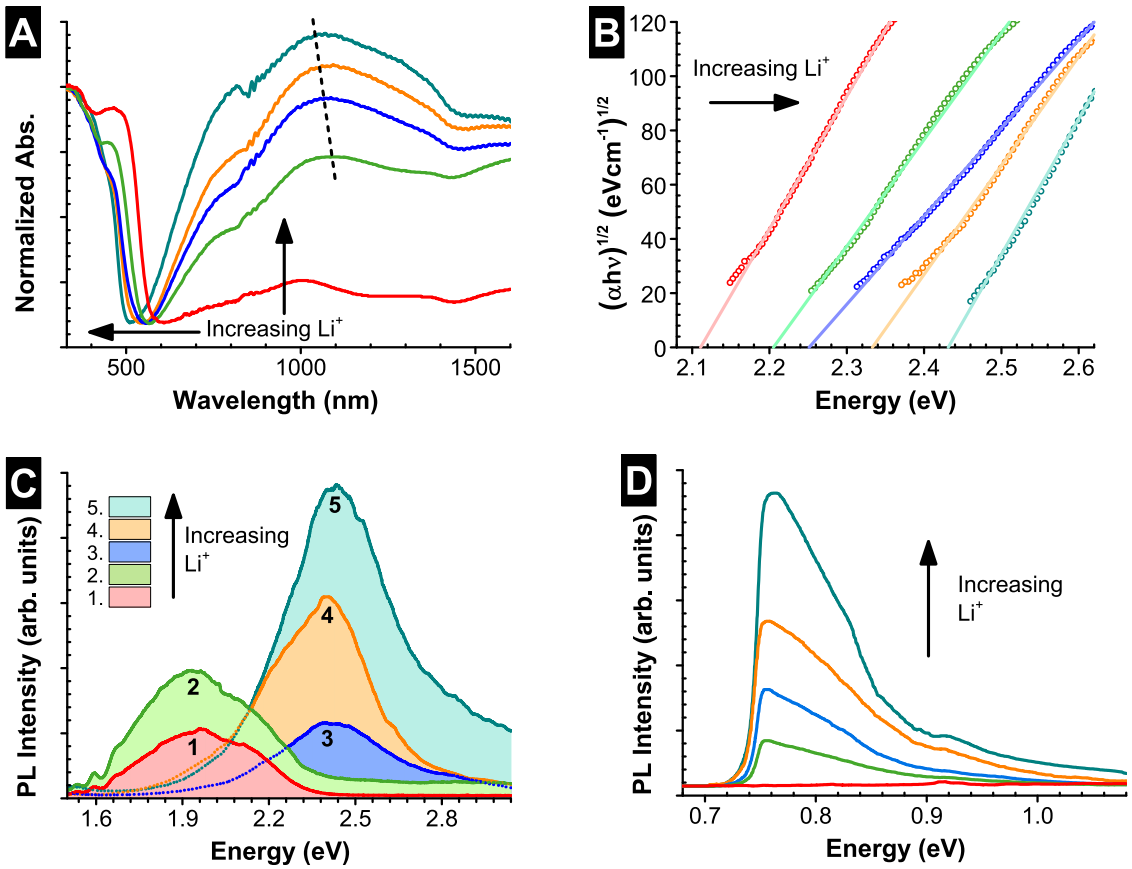

FIG. 3. Changes in the optical properties of V_2O_5 with increasing concentration of Li^+ corresponding to a electrochemical bias of OCP, 3.2, 3.0, 2.5, and 1.5 V vs Li/Li^+, respectively. Burstein-Moss shift of the optical absorbance spectra as a result of increasing concentration of Li^+ insertion: (A) the blueshift of the absorption edge from 570 to 495 nm, (B) increase in the value of optical band gap from 2.1 to 2.45 eV as estimated from the Tauc plot, and the rise in NIR absorbance peak at ~1200 nm that also shows a small blueshift of 50 nm with increasing Li^+ concentration. The dotted line on the spectra is a guide to the eye. (C) Shift in the band-edge PL emission of V_2O_5 from 1.95 to 2.45 eV with increasing Li^+ concentration in the lattice. (D) Rise in the intensity of defect-related NIR emission as a result of Li^+ insertion at various electrochemical potentials.

and δ-483 cm^{-1} are assigned to the double-coordinated oxygen (V-O2), and the triple-bridging oxygen can be identified by peaks at ν-528 cm^{-1} and δ-304 cm^{-1}. Low frequency peaks located at 103, 145, and 198 cm^{-1} correspond to the external vibrational modes. All Raman peaks are in good agreement with previously published data for orthorhombic α-V_2O_5 [50,51]. Evolution of Raman bands of V_2O_5 upon reaction with Li^+ at various electrochemical potentials is shown in Fig. S2 in the Supplemental Material [36]. Intensities of all Raman features decrease to various extents with increasing amount of Li^+ ions in the lattice, which could be due to several effects. For example, increasing structural disorder could lead to the reduction in the overall intensity of the Raman peaks, which may be especially true at high Li^+ concentration in V_2O_5. Lithium insertion also leads to changes in the color of V_2O_5 samples with a strong increase in the absorption coefficient at visible and IR spectral regions [Fig. 3(A)] as a result of defect formation that leads to a smaller Raman scattering cross-section. Absorption of both the incident and scattered light by these defects causes a reduction in the sampling depth and, hence, a reduction in the intensity of the Raman signal observed for a given concentration of V_2O_5 [52]. Curve *b* in Fig. 2(B) represents the Raman spectra taken at a potential of 3.2 V. The comparative changes in the intensity of stretching modes of each of three V-O bonds as a result of reaction with Li^+ is summarized in Table S1 in the Supplemental Material [36]. Comparison of curve *b* to curve *a* shows that the intensity of Raman peaks at 528 cm^{-1}, which corresponds to vanadium bonded to threefold coordinated oxygen (O3), changed 10% due to reaction with Li^+, whereas the characteristic bands of double-coordinated bridging oxygen, V-O2 changed 2% while the vanadyl oxygen (V = O1) remains practically unaltered with only 0.5% change. The rapid decrease in the band intensity of V-O3 over V = O1 indicates that the O3 is the oxygen atom that most readily participates in the oxidation reaction with Li^+ to form Li_2O. Both theoretical [11,41] and experimental reports [16,53] on the gas-phase catalytic studies in the literature allude to vanadyl oxygen V = O(1) as being the most active during catalytic reactions at high temperature. Our results, on the other hand, indicate that vacancies associated with O3 are the ones most readily formed under electrochemical conditions at room temperature, which is in line with the IR spectroscopic results of Ramirez *et al.* [19], and thus are most likely to play an important role in many

catalytic reactions over V_2O_5 surfaces. It must be stressed that Li^+ insertion into V_2O_5 leads to structural distortions that result in complex phase transformations (α-,ε-,δ-,γ-$Li_xV_2O_5$) that have varying electronic structures and hence vibrational dynamics. Recently, Smirnov *et al.* [54] studied the structure, electronic states, and vibrational dynamics of γ-LiV_2O_5 by combined use of quantum-chemical calculations and Raman spectroscopy and showed the lengthening of the vanadyl V-O1 bonds in the lithiated structure. The phase transformation due to Li intercalation was shown to significantly change the Raman spectrum that included formation of new intense Raman peaks at 737 and 462 cm^{-1} resulting from increase of asymmetry of the V-O3-V bridges that leads to the transformation of the asymmetric and symmetric V-O3-V vibrations into V-O3 bond stretching vibrations. These results show that straightforward comparative analysis of the Raman spectrum of pristine and lithiated V_2O_5 is inaccurate. In this paper, however, comparison of Raman intensities of various V-O bonds was done between pristine V_2O_5 and V_2O_5 reduced at 3.2 V vs Li/Li^+. Though the formation of ε-Li V_2O_5 occurs at ~3.1 V, the lithiated phases of LiV_2O_5 (α, ε, δ) at low Li^+ concentration (or high voltages) are structurally very similar to the α-V_2O_5 polymorph. The changes in the V-O bond lengths at such low Li^+ concentration is minimal, as evidenced by the absence of frequency shifts in the various V-O stretching vibrations seen in the two spectra. Hence, we believe that the Raman scattering cross-section in both cases is nearly the same (minimal changes in absorption coefficient), as evidenced by the similar band widths and shapes. However, this assumption fails at higher Li^+ loading in V_2O_5, where dramatic decreases in the intensity of Raman signals were observed.

Injection of Li^+ and e^- into metal oxide during electrochemical reduction results in the formation of LiO or Li_2O [5,48,55], as observed previously by both *in situ* transmission electron microscopy [56] and *ex situ* x-ray diffraction (XRD) measurements [57] and confirmed in this paper by XPS. The XPS spectrum of the Li 1*s* peak at the binding energy (BE) of 55.5 eV corresponds to Li_2O and is shown in Fig. S3 in the Supplemental Material [36]. The formation of the Li_2O results in a V_O defect and decrease in the oxidation state of V^{+5} to V^{+4} or lower states that was also monitored via XPS. The change in the valence state is a result of charge transfer from the defect to the neighboring vanadium atoms. The XPS spectra of the V 2*p* core level emission peaks of stoichiometric (curve *a*) and lithiated phases (curves *b* and *c*) of V_2O_5, biased at potentials of 3.2 and 2.5 V, are shown in Fig. 2(C). The binding energies of the V 2*p* levels are 516.9 and 524.5 eV for V $2p_{3/2}$ and V $2p_{1/2}$, respectively, and that of the O 1*s* level is 529.6 eV (not shown). With increasing lithiation, the spectra (*b* and *c*) show the broadening of V $2p_{3/2}$ and V$2p_{1/2}$ peaks and a shift to lower BE. In addition, a new shoulder peak at a BE of 515.8 eV appears on the low BE side of V $2p_{3/2}$, which corresponds to V^{+4}, and whose intensity increases with increasing Li^+ in the crystal. The decrease in the BE of the core level (chemical shift) indicates a decrease in the positive charge of the vanadium atom. The presence of V_O defects gives rise to new electronic states within the band gap that was evident both from the VB spectra at lower BE [shown in Fig. 2(D)] that shows the appearance of a broad peak centered at 1.3 eV above the VB edge in the lithiated sample (curves *b* and *c*) and the NIR PL emission results [Fig. 3(D)] that are discussed later.

The spectral absorption properties of pristine and lithiated V_2O_5 nanowires were measured *ex situ* in the wavelength range of 300–2600 nm in diffuse reflectance mode with $BaSO_4$ powder as the reference. The nanowire powder was scraped from the FTO substrate postlithiation and deposited on a $BaSO_4$ pellet for diffuse reflectance measurements. Care was taken to minimize air exposure before measurements. To elucidate the effects of band gap shifts with Li^+ insertion, spectra were corrected for baseline absorbance and normalized to the peak absorbance value. The normalized absorbance spectrum recorded after electrochemical reduction at various potentials w.r.t. Li/Li^+ is shown in Fig. 3(A). The absorbance of the pristine sample increases monotonically with decreasing wavelength from $\lambda = 570$ nm, which is consistent with the transition across the indirect band gap of 1.95 eV between *R* to Γ symmetry points in the Brillouin zone [35]. Lithiated V_2O_5 shows absorption peaks both in the visible as well as NIR regions. With progressive Li^+ intercalation, the optical absorption edge in the short wavelength region shifts from $\lambda = 570$ nm under no bias to $\lambda = 495$ nm when biased to 1.5 V vs Li/Li^+. The values of band gap estimated from the Tauc plot [see Fig. 3(B)] shows a corresponding increase from 2.10 to 2.45 eV. In addition to the changes in the absorbance in the short wavelength region, the absorbance in the NIR region also increased with increasing Li^+ intercalation. The unbiased sample showed no NIR absorbance, while the sample biased at negative potential showed an NIR absorption peak in the spectral range of 1000–1500 nm. With increasing Li^+ concentration, not only does the peak intensity of NIR absorbance increase, but also the peak position shifts to shorter wavelength, i.e. from $\lambda = 1500$ nm under no bias to $\lambda = 1050$ nm when biased to 1.5 V vs Li/Li^+. These changes in both band gap and NIR absorbance are consistent with the double electrochromic effect of V_2O_5 observed by previous researchers [7,20], wherein the oxide shows anodic electrochromic effect in the near-UV region, i.e. its transmission increases with lithiation, and a cathodic electrochromic effect in the NIR region where its transmittance decreases with lithiation.

Change in the PL emission in the UV-to-NIR spectral region was measured *in situ* during electrochemical reduction and is shown in Figs. 3(C) and 3(D). Spectra in the UV-to-visible region were obtained using He-Cd laser at optical excitation wavelength of $\lambda = 325$ nm. As stated earlier, V_2O_5 is an easily reducible oxide, and irradiation with even moderate energy UV or electron probe beams during measurements can easily cause oxygen desorption from the lattice. To avoid forming V_O defects during PL measurements, spectra in the NIR region were taken using a subband gap He-Ne laser at an excitation wavelength of 633 nm. Care was taken to minimize laser heating. As seen from Figs. 3(C) and 3(D), stoichiometric V_2O_5 shows a PL emission peak at 1.95 eV and no emission in the NIR spectral region. At low concentration of Li^+ intercalated into the lattice, such as when the sample is biased to 3.2 V vs Li/Li^+, the intensity of peak PL emission at 1.95 eV increases. However, at potentials more negative than 3.2 V, the peak PL emission shifts to a higher energy centered at 2.45 eV. Concomitantly, a new spectral feature in the

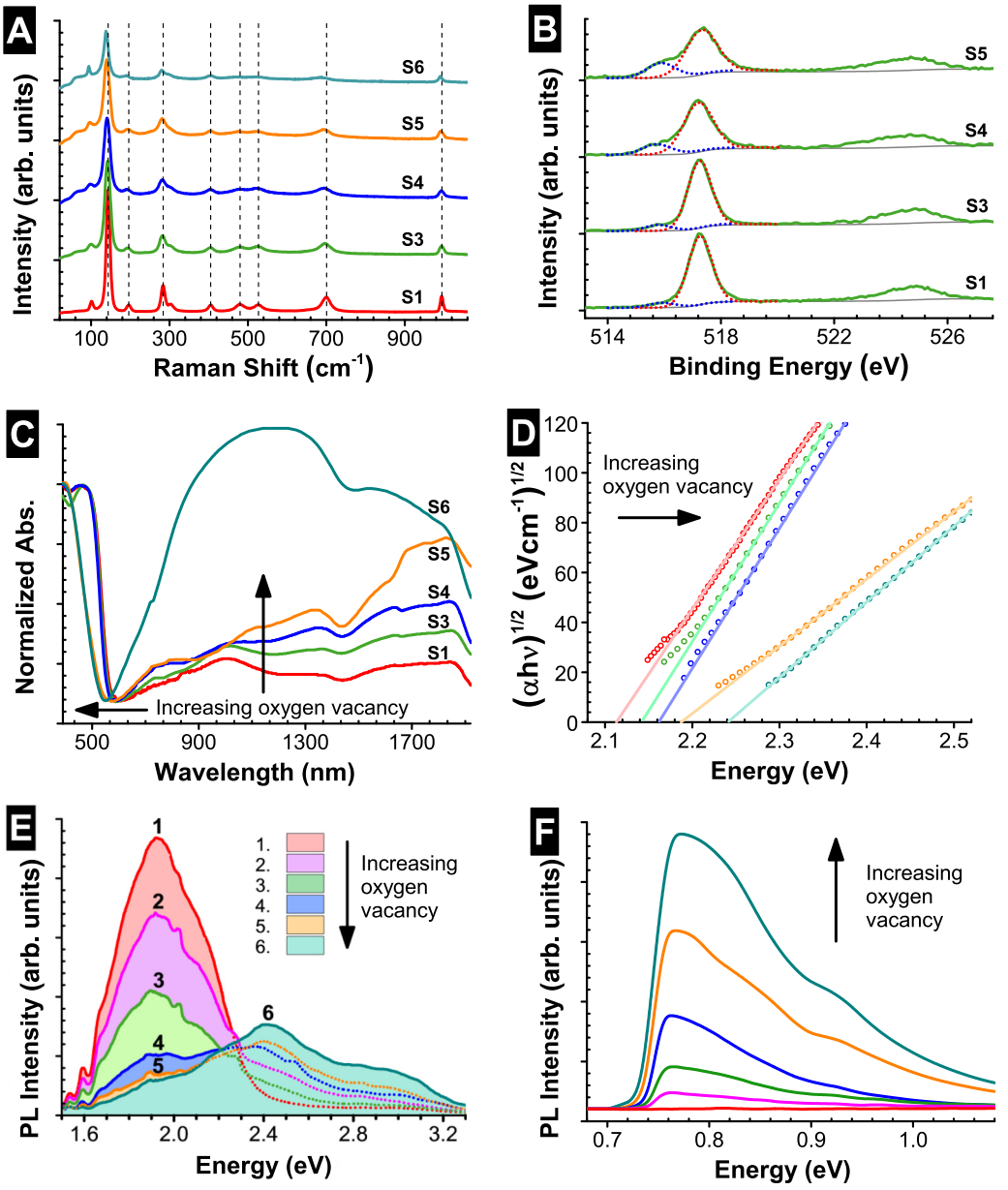

FIG. 4. Changes in the composition and optical properties of V_2O_5 as result of thermal reduction. (A) Raman spectra of oxidized (sample S1) and thermally reduced phases (samples S3–S6) of α-V_2O_5. (B) VB XPS spectra of V 2p core level of oxidized (sample S1) and thermally reduced phases (samples S3–S5). (C) Changes in the optical absorbance as a result of increasing oxygen vacancy V_O defects in the lattice: (i) The blueshift of the absorption edge from 570 to 520 nm and (D) the value of optical band gap from 2.1 to 2.25 eV, as estimated from the Tauc plot, are a result of the Burstein-Moss effect. (ii) Increase in NIR absorbance in the spectral range of 1100–1700 nm. (E) Shift in the band-edge PL emission of V_2O_5 from 1.95 to 2.45 eV with increasing V_O concentration. (F) Increase in the intensity of defect-related NIR emission with increasing number of V_O defects. Stoichiometric samples show no NIR emission.

NIR range develops whose peak emission lies at energy $E = 0.75$ eV. From Fig. 3(D), it can be seen that the intensity of this NIR emission increases with decreasing electrochemical potential, which corresponds to increasing Li^+ concentration in V_2O_5.

Like electrochemical reduction, thermal reduction of V_2O_5 during growth generates V_O defects that have a profound effect on the optical properties, as shown in Fig. 4. The concentration of V_O defects determines the stoichiometry and the crystal structure of the reduced phase. All samples, S2 to S6, of reduced oxide showed the characteristic Raman features of either V_2O_5 or V_6O_{13} or both, as shown in Fig. 3(A). Table S2 in the Supplemental Material [36] summarizes the nature of various Raman peak positions for V_6O_{13}, VO_2, and V_2O_5 as given in Ref. [50]. Note that the vibrational stretches of both V_6O_{13} and V_2O_5 occur at nearly the same wave numbers but shifted by a value of 8–10 cm^{-1}. This similarity in the spectra is due to the similarity of the structural units which form the crystals. Both crystallographic phases consist of layers of VO_6 octahedron that are relatively weakly bonded to each other. Comparison of expected peak to the measured Raman peaks in the oxidized and reduced phase indicates that samples

S1, S2 (yellow coloration), and S3 (dark-yellow coloration) were pure phases of V_2O_5. Samples S4 (brown coloration) and S5 (dark-green coloration) showed mixed phases of V_2O_5 and V_6O_{13}. Sample S6 (black coloration) was predominantly V_6O_{13}. This was further confirmed by XRD patterns from the reduced samples (S4 and S6), which is shown in Fig. S4 in the Supplemental Material [36]. The changes in the stoichiometry of the samples as a result of reduction was determined from the background corrected XPS spectra of the V $2p_{3/2}$ peak shown in Fig. 4(B). The removal of the originally negatively charged oxygen ion as a neutral species leads to the transfer of electrons to the neighboring vanadium and changes in the oxidation state of vanadium in the vicinity of the vacancy defect from V^{+5} to V^{+4}. The increase in the intensity of V^{+4} BE peak is evident in the XPS spectra of reduced samples (S3–S5) compared to the fully oxidized sample (S1) that shows no appreciable signal corresponding to V^{+4}. From the ratio of integrated intensity of V^{+5} to V^{+4}, the concentration of V^{+4} relative to V^{+5} in the reduced phases was estimated and is summarized in Table S3 in the Supplemental Material [36]. The formation of midgap states as a result of V_O was monitored at the low-BE valence spectra that are shown in the Fig. S5 in the Supplemental Material [36], which shows the development of a new peak at ~1 eV above the VB maximum in nonstoichiometric samples. The V_O defect-induced changes in the absorbance and PL emission were measured and are shown in Figs. 4(C)–4(F). Similar to changes induced by Li^+, increasing the concentration of V_O defects in the crystal causes a blueshift of the optical absorption edge from 570 to 520 nm along with the increase in the absorbance in the NIR spectral range from 1200 to 1700 nm. From the Tauc plot [Fig. 4(D)], the shift in the band gap was calculated to be from 2.1 to 2.25 eV between sample S1 (orange, V_2O_5) and sample S6 (black, V_2O_{5-x}). Similarly, the energetic position of band-edge PL emission shifts from 1.95 to 2.45 eV between stoichiometric (S1–S3) and reduced oxides (S4–S6), as shown in Fig. 4(E). The presence of V_O defects also gives rise to NIR emission peak centered at 0.75 eV, whose intensity increases with increase in concentration of defects.

The changes in the optical properties can be understood by considering the band structure of V_2O_5. Like most TMOs, the VB of V_2O_5 is derived primarily from the O $2p$ orbitals, while the CB predominantly shows the metal d band characteristics [58,59]. However, the complicated layered structure of V_2O_5 with distorted octahedrons makes the lattice effectively two dimensional and gives rise to many bands with low dispersion. In addition, the distortion leads to strong indirect V-V interactions across the intermediate bridging oxygen that links the double V-O chains in the crystal structure. As a result, the bonding part of the d band is split off from the rest of the d band and forms an intermediate d band, referred to as a "split-off" band, which lies below the main d band. Theoretical calculations of Lambrecht *et al.* [58] on the origin of the split-off band suggests that this band originates from the V $3d_{xy}$ and V $3d_{yz}$ orbitals (t_{2g} symmetry) with very small admixing from the O $2p_{xy}$ orbital. Both the absorbance edge seen at 570 nm and the PL emission at 1.95 eV indicate that stoichiometric V_2O_5 is a semiconductor with a band gap of 2.0 eV. This optical gap corresponds to the energy difference between the top of the VB derived from the O $2p$ band and the lower edge of the split-off

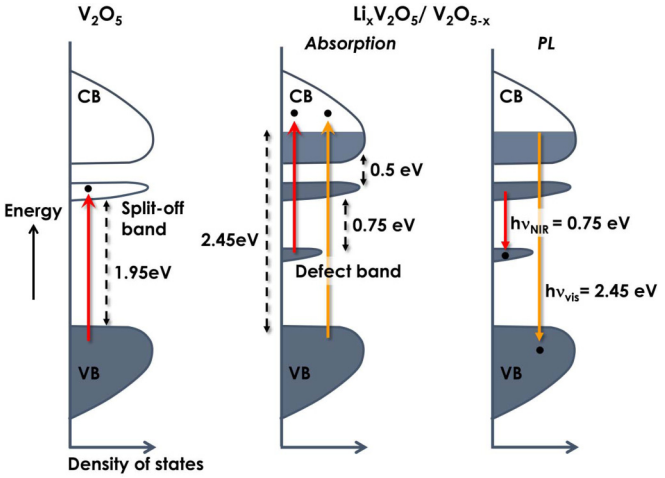

FIG. 5. Schematic of the energy band diagrams of V_2O_5, V_2O_{5-x}, and $Li_xV_2O_5$ showing the midgap energy states and the various radiative transitions resulting from the formation of oxygen vacancies for both band gap and subband gap excitations. The defect band refers to midgap states resulting from oxygen vacancy defects.

V $3d$ band that forms the CB. The Fermi level in a nominally undoped oxide lies near the lower edge of the split-off band. Optical transitions between the split-off band and the main part of the d band are parity forbidden. Stoichiometric oxide shows no NIR emission, which indicates that there are no optically measurable defect states within the band gap. The band structure and the various radiative transitions occurring upon optical excitation in both stoichiometric and reduced oxide are shown schematically in Fig. 5.

Both thermal and electrochemical reduction processes result in the generation of V_O defects and change in the oxidation state of neighboring V^{+5} atoms to V^{+4} or lower oxidation state. The formation of this defect pair creates additional electronic midgap states within the band gap. Electrochemical reduction process results in injection of e^- into the CB from the FTO back contact and insertion of Li^+ into the lattice. In thermal reduction, the neutral oxygen atoms that are being removed from the crystal donate their excess electrons to the vanadium atoms. Prior studies have indicated that these excess electrons are localized on the vanadium atoms near the vicinity of defects [11,39]. However, the shift in the optical absorption edge with increasing concentration of V_O defects suggest that the e^- are delocalized over the entire crystal and are part of the CB electrons. This e^- injection results in the filling of the split-off d band and shift in the Fermi level to a higher energy. When the concentration of conduction electron n_e is low, the Fermi level remains within the split-off d band. The slight increase in the e^- concentration results in the increase in the intensity of band edge PL emission at 1.95 eV, which is seen in both types of reduced oxide. However, with increasing n_e during progressive reduction or Li^+ intercalation, the Fermi level abruptly moves into the main part of the V $3d$ band upon complete filling of the split-off band. As a result, the optical absorption of the sample shows a shift to a lower wavelength, i.e. from 570 nm in the pristine sample to 495 nm. This optical shift in the absorption edge to higher energy as a result of band filling is referred to as the Burstein-Moss effect. The optical transitions then occur

between the top of the O $2p$ VB and the bottom of the main V $3d$ band. The abrupt shift in the peak position of PL emission from 1.95 to 2.45 eV indicates that the energetic position of the split-off band is ~0.5 eV below the main d band, which is consistent with the results of both theoretical calculation [58] and prior optical absorption studies [20]. As mentioned earlier, this increase in the optical band gap as a result of V_2O_5 reduction is unexpected because the band gap of most oxide decreases with increasing oxygen vacancy or formation of metal d band DOS within the band gap [60], including vanadium oxide whose band gap narrows from 2.0 to 0.7 eV in VO_2 to 0.4 eV in V_2O_3 and no gap in VO. The evolution of increasing DOS within the forbidden gap and narrowing of the gap in reduced vanadium oxide has been observed by photoemission studies [15]. Interestingly, thermal reduction in other n-type TMOs, such as WO_3 or MoO_3, leads to increase in n-type conductivity with e^- injection into the CB; however, they show no shift in the optical band gap [32]. The blueshift seen in V_2O_5 may be a consequence of the low dispersion of CB states, which leads to band filling even with relatively small concentration of e^- injection.

From the energetic position of the NIR emission peak of both V_2O_{5-x} and $Li_xV_2O_5$, and from the fact that presence of V_O defects induces n-type conductivity in V_2O_5, it can be concluded that V_O defect states are located ~0.75 eV below the split-off d band, which is consistent with the theoretical predictions of Scanlon *et al.* [11]. This band filling causes blueshift not only of the optical absorption edge, but also the peak absorbance seen in the NIR spectral range. Previous papers [20] have attributed this NIR absorption to small polaron absorption and the broadening of this absorption band with lithiation to the lattice disorder that causes electronic transitions to neighboring sites to take place at higher energy. Considering both the NIR PL emission and absorption results seen in this paper, we attribute the NIR absorption to be a result of electronic transition from the V_O defects located 0.75 eV below the split-off d band to the upper part of the main d band. The observation that NIR absorbance also blueshifts with increasing electron concentration indicates that this absorbance is a result of electronic excitations involving main d band states and supports our above conclusion. The NIR PL emission seen at 0.75 eV is a result of electron transitions between the split-off d band and the V_O defect states.

It can be argued that the changes in the optical gap of V_2O_5 seen with lithiation is not a true Burstein-Moss effect, as structural distortions and phase transformations can lead to marked changes in the Mott-Hubbard band. In this case, one can argue that the changes in the observed optical spectra be attributed to the differences in the fundamental energy band gap (E_{CB}-E_{VB}) of various lithiated phases, as opposed to the proposed explanation where changes were attributed to the increase in the optical gap (E_F-E_{VB}) with a constant energy band gap. It must be pointed out that though Li^+ insertion into V_2O_5 leads to phase transformations whose structural parameters may be markedly different from parent V_2O_5, as pointed out by Smirnov *et al.* [54] for γ-LiV_2O_5, spin-polarized DFT + U calculations, however, do not indicate shifts in the fundamental energy gap, and the major effect of lithiation on electronic structure is the formation of midgap states [11,54,61], as is observed in this paper. The similarly in the changes in the optical properties (optical band gaps increase) between electrochemically and thermally reduced V_2O_5, where marked structural phase transformation only occurs in the former case, supports the conclusion that the fundamental electronic gap remains nearly the same and the increase in the optical gap is due to Burstein-Moss effect. Finally, Fig. S5 in the Supplemental Material [36] shows the changes in the optical absorbance spectra as a result of Li^+ insertion into a reference n-type sample, tungsten oxide (WO_3). While the rise in the NIR absorbance peak at ~1200 nm in Li_xWO_3, which indicates the formation of V_O defects as a result of Li^+ insertion, is similar to that seen in $Li_xV_2O_5$, unlike in V_2O_5 that shows Burstein-Moss in the optical gap, no blueshift of the absorption edge is seen in WO_3 with Li^+ insertion.

In summary, we show here the main effects of oxygen vacancy defects on the electronic and optical properties of V_2O_5 nanowires through *in situ* Raman PL, absorption, and photoemission spectroscopy. Both thermal and electrochemical reduction of V_2O_5 leads to creation of oxygen vacancy defects with the delocalization and injection of excess electrons into the CB, as opposed to localized electron injection as previously suggested. Vacancy formation also gives rise to new electronic midgap defect states that lie ~0.75 eV below the split-off d band. Band filling with excess electrons leads to Burstein-Moss shift of the optical absorption edge and PL emission from 1.95 to 2.45 eV. This increase in the optical band gap is contrary to that seen in most oxides, where reduction leads to decrease in the band gap. Further, *in situ* Raman measurements during the reduction process show that the oxygen atom that most readily reacts during room temperature electrochemical reduction is the threefold coordinated oxygen (O3).

The authors gratefully acknowledge the financial support of a National Science Foundation grant (CBET, Award No: 1511733) and the Rensselaer Polytechnic Institute through the Howard P. Isermann fellowship for Q.W., M.B., S.J., and A.P.

APPENDIX: METHODS AND MATERIALS

1. Synthesis of V_2O_5 nanostructures

Nanowires of various stoichiometries were synthesized by HFCVD in a custom-built quartz reactor. Detailed description of the reactor and the technique can be found in our previous paper [32]. A 0.5 mm diameter vanadium wire was resistively heated to filament temperatures of 1000–1500 K using a variable voltage power supply. The reaction of oxygen with the hot vanadium filament results in the formation of vanadium oxide. Deposition on different substrates was done by placing them approximately 5 mm below the filament during growth. Substrate temperatures during growth were in the range of 500–800 K. Fluorine-doped tin oxide (FTO) coated glass served as the substrates for most of electrical measurements. Prior to deposition, substrates were cleaned sequentially with soapy water, acetone, ethanol, and deionized water and dried under nitrogen. Deposition was carried out under oxygen or oxygen mixed with humid air at a reactor pressure of 1 torr. Stoichiometry of the oxide was controlled by modulating the total power delivered to the filament and the composition of

the gas phase species. Stoichiometric V_2O_5 deposit (sample S1) was obtained under pure oxygen atmosphere. Introduction of humid air into the reactor and higher filament temperature promoted the formation of reduced phases of V_2O_5 (samples S2 to S6).

2. Characterization

The morphology of the samples was examined by SEM (Carl Zeiss SUPRA 55 FESEM). The composition and structure of V_2O_5 were characterized by XRD (PANalytical X'Pert Pro Diffractometer) and XPS (Physical Electronics PHI 5000 VersaProbe). X-ray photoemission spectroscopy measurements were carried out at room temperature in a UHV system with a base pressure of 10^{-9} mbar. Al Kα radiation ($h\nu = 1486.6$ eV) from a monochromatic x-ray source was used for excitation. The spectra are given in BE referenced to the Fermi level of a sputter cleaned Au reference sample.

3. Optical absorption measurements

Absorbance (A) of the V_2O_5 samples were recorded in the diffuse reflectance mode using a UV-visible-NIR spectrophotometer (Shimadzu UV-3600) in the range of 300–2600 nm. For each measurement, samples were scraped off from the substrate and then uniformly spread onto a layer of barium sulfate ($BaSO_4$) powder that served as the reflectance standard. The band gap of the material was determined from the Tauc plot, which is given by the relationship [33]

$$(h\nu\alpha)^{1/n} = B\,(h\nu - E_g),$$

where h is the Planck's constant, ν is frequency, α is the absorption coefficient, B is a proportionality constant, and n denotes the nature of the allowed transitions, $n = 1/2$ for direct and $n = 2$ for indirect transitions. The optical band gap was estimated by taking the intercept of the extrapolation of the tangent line to the linear portion of the curve to the inflection point of the x axis.

In situ Raman and PL measurements were performed with a HORIBA Scientific LabRAM HR Evolution spectrometer. Raman spectra were acquired at room temperature using the 633 nm line of a helium-neon laser at a laser power of 16 mW. Band gap PL measurements in the energy range of 3.8 to 1.2 eV were done using a 325 nm excitation energy of a He-Cd laser. Near-IR PL spectra were recorded in the 0.7–1.8 eV range using a liquid nitrogen-cooled InGaAs charge-coupled detector at an excitation wavelength of 633 nm. All measurements were done at room temperature. Care was taken to avoid laser heating of the sample. For *in situ* measurements, a small stainless steel electrochemical cell with a quartz window was constructed.

4. Electrochemical studies

Here, Li^+ insertion into V_2O_5 was performed in a glove box under argon atmosphere using a standard three-electrode setup that consisted of Li metal (MTI Corp) as both the counter and reference electrodes. The composition of the electrolyte was 0.1 M lithium perchlorate ($LiClO^4$, Aldrich, 99.99%) in anhydrous propylene carbonate (PC, Sigma-Aldrich, 99.7%). The intercalation process was done with application of constant step potential in the range of 3.2–0.5 V vs Li/Li^+ using a Zahner IM6 electrochemical workstation, and allowed to reach equilibrium that took approximately 3–5 h. For absorption measurements, samples were immersed from the electrolyte and dried completely inside the glove box before each run.

[1] E. A. Mamedov and V. Cortés Corberán, Oxidative dehydrogenation of lower alkanes on vanadium oxide-based catalysts. The present state of the art and outlooks, Appl. Catal., A **127**, 1 (1995).

[2] P. Mars and D. W. van Krevelen, Oxidations carried out by means of vanadium oxide catalysts, Chem. Eng. Sci. **3**, 41 (1954).

[3] F. Amano, T. Tanaka, and T. Funabiki, Steady-state photocatalytic epoxidation of propene by O2 over V_2O_5/SiO_2 photocatalysts, Langmuir **20**, 4236 (2004).

[4] G. C. Bond and S. F. Tahir, Vanadium oxide monolayer catalysts preparation, characterization and catalytic activity, Appl. Catal. **71**, 1 (1991).

[5] L. Ji, Z. Lin, M. Alcoutlabi, and X. Zhang, Recent developments in nanostructured anode materials for rechargeable lithium-ion batteries, Energy Environ. Sci. **4**, 2682 (2011).

[6] J. Liu, X. Wang, Q. Peng, and Y. Li, Vanadium pentoxide nanobelts: Highly selective and stable ethanol sensor materials, Adv. Mater. **17**, 764 (2005).

[7] F. Yoshitaka, M. Katsuhiro, and T. Chiei, On the electrochromism of evaporated V_2O_5 films, Jpn. J. Appl. Phys. **24**, 1082 (1985).

[8] B. Grzybowska-Świerkosz, Vanadia catalysts for selective oxidation of hydrocarbons and their derivatives: Active centres on vanadia-based catalysts for selective oxidation of hydrocarbons, Appl. Catal., A **157**, 409 (1997).

[9] R.-P. Blum, H. Niehus, C. Hucho, R. Fortrie, M. V. Ganduglia-Pirovano, J. Sauer, S. Shaikhutdinov, and H.-J. Freund, Surface Metal-Insulator Transition on a Vanadium Pentoxide (001) Single Crystal, Phys. Rev. Lett. **99**, 226103 (2007).

[10] S. Laubach, P. C. Schmidt, F. J. Thi Fernandez-Madrigal, Q.-H. Wu, W. Jaegermann, M. Klemm, and S. Horn, Theoretical and experimental determination of the electronic structure of V_2O_5, reducedV_2O_5-x and sodium intercalated NaV_2O_5, Phys. Chem. Chem. Phys. **9**, 2564 (2007).

[11] D. O. Scanlon, A. Walsh, B. J. Morgan, and G. W. Watson, An *ab initio* study of reduction of V_2O_5 through the formation of oxygen vacancies and Li intercalation, J. Phys. Chem. C **112**, 9903 (2008).

[12] M. Vanhaelst, and P. Clauws, EPR spectrum of the oxygen vacancy in single crystals V_2O_5, Phys. Stat. Sol. B **87**, 719 (1978).

[13] R. Zimmermann, P. Steiner, R. Claessen, F. Reinert, S. Hüfner, P. Blaha, and P. Dufek, Electronic structure of 3*d*-transition-metal oxides: On-site Coulomb repulsion versus covalency, J. Phys. Condens. Matter **11**, 1657 (1999).

[14] W. Lambrecht, B. Djafari-Rouhani, and J. Vennik, Theoretical study of the vanadyl-oxygen vacancy in V_2O_5: Tight-binding Green function calculation, optical properties and neutral vacancy ground-state splitting, J. Phys. C **19**, 369 (1986).

[15] M. Demeter, M. Neumann, and W. Reichelt, Mixed-valence vanadium oxides studied by XPS, Surf. Sci. **454–456**, 41 (2000).

[16] E. Gillis and E. Boesman, E.P.R.-studies of V_2O_5 single crystals. I. Defect centres in pure, non-stoichiometric vanadium pentoxide, Phys. Status Solidi B **14**, 337 (1966).

[17] Q.-H. Wu, A. Thissen, W. Jaegermann, and M. Liu, Photoelectron spectroscopy study of oxygen vacancy on vanadium oxides surface, Appl. Surf. Sci. **236**, 473 (2004).

[18] K. Hermann, M. Witko, R. Druzinic, A. Chakrabarti, B. Tepper, M. Elsner, A. Gorschlüter, H. Kuhlenbeck, and H. J. Freund, Properties and identification of oxygen sites at the V_2O_5(010) surface: Theoretical cluster studies and photoemission experiments, J. Electron. Spectrosc. Relat. Phenom. **98**, 245 (1999).

[19] R. Ramirez, B. Casal, L. Utrera, and E. Ruiz-Hitzky, Oxygen reactivity in vanadium pentoxide: electronic structure and infrared spectroscopy studies, J. Phys. Chem. **94**, 8960 (1990).

[20] A. Talledo and C. G. Granqvist, Electrochromic vanadium-pentoxide-based films: Structural, electrochemical, and optical properties, J. Appl. Phys. **77**, 4655 (1995).

[21] S. F. Cogan, N. M. Nguyen, S. J. Perrotti, and R. D. Rauh, Optical properties of electrochromic vanadium pentoxide, J. Appl. Phys. **66**, 1333 (1989).

[22] Q.-H. Wu, A. Thißen, and W. Jaegermann, Photoelectron spectroscopic study of Li intercalation into V_2O_5 thin films, Surf. Sci. **578**, 203 (2005).

[23] B. Pecquenard, D. Gourier, and D. Caurant, Electron nuclear double resonance of polarons in α-$Li_xV_2O_5$, J. Phys. Chem. **100**, 9152 (1996).

[24] J. Jiang, Z. Wang, and L. Chen, Structural and electrochemical studies on β-$Li_xV_2O_5$ as cathode material for rechargeable lithium batteries, J. Phys. Chem. C **111**, 10707 (2007).

[25] S. Shin, Y. Tezuka, T. Kinoshita, A. Kakizaki, T. Ishii, Y. Ueda, W. Jang, H. Takei, Y. Chiba, and M. Ishigame, Observation of local magnetic moments in the Mott transition of V_2O_3 by means of 3s photoemission, Phys. Rev. B **46**, 9224 (1992).

[26] R. Goschke, K. Vey, M. Maier, U. Walter, E. Goering, M. Klemm, and S. Horn, Tip induced changes of atomic scale images of the vanadium pentoxide surface, Surf. Sci. **348**, 305 (1996).

[27] T. Oshio, Y. Sakai, and S. Ehara, Scanning tunneling microscopy/spectroscopy study of V_2O_5 surface with oxygen vacancies, J. Vac. Sci. Technol., B **12**, 2055 (1994).

[28] N. Pinna, M. Willinger, K. Weiss, J. Urban, and R. Schlögl, Local structure of nanoscopic materials: V_2O_5 nanorods and nanowires, Nano Lett. **3**, 1131 (2003).

[29] D. S. Su, M. Wieske, E. Beckmann, A. Blume, G. Mestl, and R. Schlögl, Electron beam induced reduction of V_2O_5 studied by analytical electron microscopy, Catal. Lett. **75**, 81 (2001).

[30] D. S. Su, H. W. Zandbergen, P. C. Tiemeijer, G. Kothleitner, M. Hävecker, C. Hébert, A. Knop-Gericke, B. H. Freitag, F. Hofer, and R. Schlögl, High resolution EELS using monochromator and high performance spectrometer: Comparison of V_2O_5 ELNES with NEXAFS and band structure calculations, Micron **34**, 235 (2003).

[31] Q. Wang, A. Puntambekar, and V. Chakrapani, Vacancy-induced semiconductor-insulator-metal transitions in non-stoichiometric nickel and tungsten oxides, Nano Lett. **16**, 7067 (2016).

[32] V. Chakrapani, M. Brier, A. Puntambekar, and T. DiGiovanni, Modulation of stoichiometry, morphology and composition of transition metal oxide nanostructures through hot wire chemical vapor deposition, J. Mater. Res. **31**, 17 (2016).

[33] V. Chakrapani, J. Thangala, and M. K. Sunkara, WO_3 and W_2N nanowire arrays for photoelectrochemical hydrogen production, Int. J. Hydrogen Energy **34**, 9050 (2009).

[34] D. R. Lide, *CRC Handbook of Chemistry and Physics* (Chemical Rubber Co., Boca Raton, 2003).

[35] W. Lambrecht, B. Djafari-Rouhani, M. Lannoo, P. Clauws, L. Fiermans, and J. Vennik, The energy band structure of V_2O_5. II. Analysis of the theoretical results and comparison with experimental data, J. Phys. C **13**, 2503 (1980).

[36] See Supplemental Material at http://link.aps.org/supplemental/10.1103/PhysRevB.94.245305 for the changes in Raman, XRD, XPS and optical absorbance spectra before and after thermal and electrochemical reduction of V_2O_5.

[37] D. Göbke, Y. Romanyshyn, S. Guimond, J. M. Sturm, H. Kuhlenbeck, J. Döbler, U. Reinhardt, M. V. Ganduglia-Pirovano, J. Sauer, and H.-J. Freund, Formaldehyde formation on vanadium oxide surfaces V_2O_3 (0001) and V_2O_5 (001): How does the stable methoxy intermediate form? Angew. Chem., Int. Ed. **48**, 3695 (2009).

[38] J. M. Sturm, D. Göbke, H. Kuhlenbeck, J. Döbler, U. Reinhardt, M. V. Ganduglia-Pirovano, J. Sauer, and H.-J. Freund, Partial oxidation of methanol on well-ordered V_2O_5 (001)/Au (111) thin films, Phys. Chem. Chem. Phys. **11**, 3290 (2009).

[39] A. Chakrabarti, K. Hermann, R. Druzinic, M. Witko, F. Wagner, and M. Petersen, Geometric and electronic structure of vanadium pentoxide: A density functional bulk and surface study, Phys. Rev. B **59**, 10583 (1999).

[40] B. Tepper, B. Richter, A.-C. Dupuis, H. Kuhlenbeck, C. Hucho, P. Schilbe, M. A. bin Yarmo, and H.-J. Freund, Adsorption of molecular and atomic hydrogen on vacuum-cleaved V_2O_5 (001), Surf. Sci. **496**, 64 (2002).

[41] W. Lambrecht, B. Djafari-Rouhani, and J. Vennik, Electronic structure of bulk and surface vanadyl oxygen vacancies in the layer compound V_2O_5, Surf. Sci. **126**, 558 (1983).

[42] U. S. Ozkan, Y. P. Cai, M. W. Kumthekar, and L. P. Zhang, Role of ammonia oxidation in selective catalytic reduction of nitric oxide over vanadia catalysts, J. Catal. **142**, 182 (1993).

[43] M. Calatayud, and C. Minot, Reactivity of the oxygen sites in the V_2O_5/TiO_2 anatase catalyst, J. Phys. Chem. B **108**, 15679 (2004).

[44] B. M. Weckhuysen, J.-M. Jehng, and I. E. Wachs, *In situ* Raman spectroscopy of supported transition metal oxide catalysts: $^{18}O_2$-$^{16}O_2$ isotopic labeling studies, J. Phys. Chem. B **104**, 7382 (2000).

[45] E. L. Lee and I. E. Wachs, *Insitu* Raman spectroscopy of SiO_2-supported transition metal oxide catalysts: An isotopic ^{18}O-^{16}O exchange study, J. Phys. Chem. C **112**, 6487 (2008).

[46] S. Xie, E. Iglesia, A. T. Bell, Effects of hydration and dehydration on the structure of silica-supported vanadia species, Langmuir **16**, 7162 (2000).

[47] I. Muylaert, and P. Van DerVoort, Supported vanadium oxide in heterogeneous catalysis: Elucidating the structure—Activity relationship with spectroscopy, Phys. Chem. Chem. Phys. **11**, 2826 (2009).

[48] M. Smirnov, and R. Baddour-Hadjean, Li intercalation in TiO_2 anatase: Raman spectroscopy and lattice dynamic studies, J. Chem. Phys. **121**, 2348 (2004).

[49] M. Banares, and I. Wachs, Molecular structures of supported metal oxide catalysts under different environments, J. Raman Spec. **33**, 359 (2002).

[50] C. Julien, G. A. Nazri, and O. Bergström, Raman scattering studies of microcrystalline V_6O_{13}, Phys. Status Solidi B **201**, 319 (1997).

[51] R. Baddour-Hadjean, M. Smirnov, K. Smirnov, V. Y. Kazimirov, J. Gallardo-Amores, U. Amador, M. Arroyo-de Dompablo, and J. Pereira-Ramos, Lattice dynamics of β-V_2O_5: Raman spectroscopic insight into the atomistic structure of a high-pressure vanadium pentoxide polymorph, Inorg. Chem. **51**, 3194 (2012).

[52] G. Mestl, P. Ruiz, B. Delmon, and H. Knozinger, Oxygen-exchange properties of MoO_3: An *in situ* Raman spectroscopy study, J. Phys. Chem. **98**, 11269 (1994).

[53] Y. H. Kim and H.-I. Lee, Redox property of vanadium oxide and its behavior in catalytic oxidation, Bull. Korean Chem. Soc. **20**, 1457 (1999).

[54] M. B. Smirnov, E. Roginskii, V. Y. Kazimirov, K. S. Smirnov, R. Baddour-Hadjean, J.-P. Pereira-Ramos, and V. Zhandun, Spectroscopic and computational study of structural changes in γ-LiV_2O_5 cathodic material induced by lithium intercalation, J. Phys. Chem. C **119**, 20801 (2015).

[55] J. Wu, J. Cao, W. Q. Han, A. Janotti, and H. C. Kim, *Functional Metal Oxide Nanostructures* (Springer, New York, 2011).

[56] P. Poizot, S. Laruelle, S. Grugeon, L. Dupont, and J. Tarascon, Nano-sized transition-metal oxides as negative-electrode materials for lithium-ion batteries, Nature **407**, 496 (2000).

[57] W. Liu, X. Huang, Z. Wang, H. Li, and L. Chen, Studies of stannic oxide as an anode material for lithium-ion batteries, J. Electrochem. Soc. **145**, 59 (1998).

[58] W. Lambrecht, B. Djafari-Rouhani, and J. Vennik, On the origin of the split-off conduction bands in V_2O_5, J. Phys. C **14**, 4785 (1981).

[59] D. W. Bullett, The energy band structure of V_2O_5: A simpler theoretical approach, J. Phys. C **13**, L595 (1980).

[60] A. Naldoni, M. Allieta, S. Santangelo, M. Marelli, F. Fabbri, S. Cappelli, C. L. Bianchi, R. Psaro, and V. Dal Santo, Effect of nature and location of defects on bandgap narrowing in black TiO_2 nanoparticles, J. Am. Chem. Soc. **134**, 7600 (2012).

[61] R. Valentí, T. Saha-Dasgupta, J. Alvarez, K. Požgajčić, and C. Gros, Modeling the Electronic Behavior of γ-LiV_2O_5: A Microscopic Study, Phys. Rev. Lett. **86**, 5381 (2001).